10^{th} International Conference on Fracture Mechanics of Concrete and Concrete Structures
FraMCoS-X
G. Pijaudier-Cabot, P. Grassl and C. La Borderie (Eds)
https://doi.org/10.21012/FC10.232765

NEUTRON-IRRADIATION–INDUCED DAMAGE ASSESSMENT IN CONCRETE USING COMBINED PHASE CHARACTERIZATION AND NONLINEAR FAST FOURIER TRANSFOR SIMULATION

YANN LE PAPE[*], ELENA TAJUELO RODRIGUEZ[*], JOSE DAVID ARREGUI MENA[*], ALAIN GIORLA[†], LAWRENCE ANOVITZ[*] AND THOMAS M. ROSSEEL[*]

[*] Oak Ridge National Laboratory
One Bethel Valley Road, Oak Ridge TN 37831, USA
e-mail: lepapeym@ornl.gov, tajuelorodre@ornl.gov, arreguimenjd@ornl.gov, rosseeltm@ornl.gov

[‡] Formerly at Oak Ridge National Laboratory
e-mail: alain.b.giorla@gmail.com

Key words: Irradiation, Nuclear, Swelling, Damage

Abstract. Understanding irradiation effects in concrete cavities of light water reactors is critical to the long-term operation (60+ years) of US nuclear power plants. Susceptibility of concrete to neutron irradiation greatly varies as a function of its constituents: coarse aggregates, sand, and hardened cement paste (hcp). In particular, higher irradiation–susceptibility of aggregates was found to be a direct function of radiation-induced volumetric expansion (RIVE), or the propensity of aggregates to swell as a function of mineral contents, structures and textures. Irradiation-induced amorphization is accompanied by significant swelling, especially in silicates. For example, the maximum volumetric expansions of quartz and feldspars have been shown to be as large as $\approx 18\%$ and $\approx 8\%$, respectively, while the change of density in calcite remains rather low ($\approx 0.3 - 0.5\%$). High swelling is associated with a high number of covalent bonds (Si$-$O) and a high degree of polymerization of [SiO_4] tetrahedrons. Differential RIVEs between rock-forming minerals cause high stresses and may potentially develop cracking within the aggregates at the interface between aggregates and the hcp and within the hcp. Modeling neutron-irradiation effects in concrete requires addressing the problem at a scale that captures both the details of the aggregates' mineralogy and texture, which is $<\sim 100$ µm, and the representative size of concrete, which is ~ 10 cm. This requires high-resolution, large mapping capabilities. To this end, the US Department of Energy (DOE) Light Water Reactor Sustainability (LWRS) Program developed an original tool suite called Microstructure Oriented Scientific Analysis of Irradiated Concrete (MOSAIC) in which Nonlinear 2D-fast Fourier transform (FFT) techniques are employed to model mechanical or irradiation-induced cracking of high-resolution complex microstructures derived from combined mapping techniques, including micro x-ray fluorescence (m-XRF), energy-dispersive x-ray spectroscopy (EDS), electron backscatter diffraction (EBSD), ellipsometry, and scanning electron microscopy (SEM). Irradiated mineral properties are derived from the Irradiated Minerals, Aggregate and Concrete (IMAC) database, which includes available relevant literature data. Rigorous coupled damage-creep simulations are obtained through sequential linear analysis. Illustrations of actual accelerated irradiation-damage propagation in a complex microstructures are presented herein.

1 INTRODUCTION

Concrete is a heterogeneous, porous material that can be viewed as a complex assemblage of varied minerals, generally highly crystallized in the aggregates, and poorly crystallized in the hardened cement paste. The irradiation tolerance of concrete depends largely on the mineralogy and crystallinity of the minerals present in the aggregates. In particular, irradiation-induced damage is mainly governed by the radiation-induced volumetric expansion (RIVE) occurring in the aggregate-forming minerals [1, 2, 3]. The RIVE rate and amplitude vary greatly with mineralogy: silica content [4], number of ionic vs. covalent bonds, and structural percolation of the silicate tetrahedrons [5]. The coexistence of varied rock-forming minerals in concrete aggregate will result in mismatch strains, causing internal stress development and possibly irradiation-induced cracking with RIVE. The morphology and microstructural arrangement of these minerals are critical in this degradation process. Thus, determining any specific concrete's tolerance/susceptibility against irradiation in order to inform potential nuclear power plant (NPP) license renewal (LR) [6] requires a detailed characterization of its microstructure, as well as advanced modeling. To this end, the US DOE Light Water Reactor Sustainability (LWRS) Program has been developing a holistic approach centered on a numerical platform combining the Microstructure-Oriented Scientific Analysis of Irradiated Concrete (MOSAIC) for image analysis and irradiation damage simulation with experimental data from the Irradiated Minerals Aggregates and Concrete (IMAC) database.

The proposed approach is enumerated in the following logical sequence:

1. Characterization of unirradiated concrete using a suite of imaging techniques (micro x-ray fluorescence (mXRF), energy-dispersive x-ray spectroscopy (EDS), and petrography)

2. Phase identification / phase map reconstruction

3. Modeling of unirradiated and irradiated properties, and

4. Comparison/validation against experimental data on irradiated concrete.

2 MATERIALS CHARACTERIZATION

2.1 Materials

Composition ($w/c = 0.5$) [4] Water: $w = 183\ \mathrm{kg\,m^{-3}}$, high-early strength cement (Taiheiyo Cement Corp.): $c = 366\ \mathrm{kg\,m^{-3}}$ ($\rho_c = 3.14\ \mathrm{g\,cm^{-3}}$), land sand, sandstone (Shizuoka Prefecture): $s = 799\ \mathrm{kg\,m^{-3}}$ ($\rho_s = 2.61\ \mathrm{g\,cm^{-3}}$), 5–13 mm crushed altered tuff GA(A) – grain size ranging from 0.1-0.3 mm: $g = 995\ \mathrm{kg\,m^{-3}}$ ($\rho_g = 2.66\ \mathrm{g\,cm^{-3}}$). The weight fraction of cement, water, sand, and aggregate are 15.6%, 7.8%, 34.1% and 42.5%, respectively. The total occupied volume of mixed constituents is 0.979 m^3 which theoretically corresponds to 2.1% of entrapped air. The volume fractions of the sand and aggregate are respectively 31% and 38%.

Specimens Unirradiated concrete specimens were provided to Oak Ridge National Laboratory (ORNL) by the Japan Concrete Aging Management Program (JCAMP) group as 4 cm diameter cylinders 6 cm high, and the aggregate specimens were 1 cm diameter cylinders 1 cm high.

2.2 Techniques

Petrography Petrography is a standard mineral identification technique in geology using plain polarized light and cross-polarized light. Thin sections of the aggregates were mounted with epoxy resin on microscope slides and were examined using an Olympus optical microscope with a digital camera.

x-ray diffraction (XRD) X-ray diffraction pattern acquisition and Rietveld analysis were performed previously elsewhere ([7] and [4]).

micro x-ray fluorescence (mXRF) A polished slice of the concrete was scanned using an Atlas mXRF system (IXRF instruments) with a Rh x-ray source operated at a voltage of 50 kV and a current of 600 $\mu\mathrm{A}$. The irradiation was performed under vacuum (30 kPa). The x-ray maps were acquired using the following conditions: (1) spot size: 10 $\mu\mathrm{m}$; (2) width $\times$ length: 25.1 $\times$ 25.1 mm; (3) resolution: 512 $\times$ 512 pixels; (4) pixel size: 49 $\mu\mathrm{m}$; (5) time constant (internal parameter to control the count processing time): 1; (6) point dwell (time the beam spends at every pixel): 1500 ms; (7) total acquisition time: $\approx$111 h. The constitutive elements were identified according to major peaks in the sum spectra of the analyzed area. Individual elemental maps with information on counts per pixel were provided. This information was transformed into weight percentage in MOSAIC.

Energy-dispersive x-ray spectroscopy (EDS) An FEI 3D dual beam field emission SEM equipped with an X-Max 150 mm^2 silicon drift energy dispersive spectrometer detector was used to obtain all the EDS maps under the conditions given below: (1) width $\times$ length: 3.25 $\times$ 2.03 mm; (2) resolution: 2,048 $\times$ 1,280 pixels; (3) acceleration voltage 20 μV; and (4) beam current 8 μA.

3 PHASES IDENTIFICATION

Aggregate-forming minerals Petrographic analysis of a thin section of aggregate GA(A) revealed mainly quartz, which corresponds to the fine gray grains in 1. Biotite was also identified as the brown-like vein in 1.

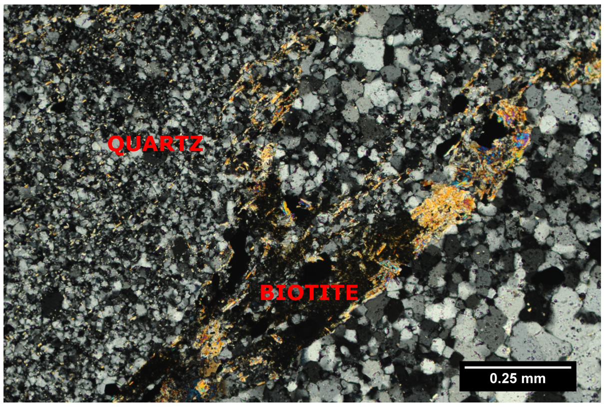

Figure 1: Petrography of aggregate GA(A) with crossed polars.

Quantitative XRD-based Rietveld analysis provided by the JCAMP research team confirmed that aggregate GA(A) has a high silica content in the form of quartz (SiO_2), with a volume fraction estimated to be 92%. The remaining minerals are primarily from the feldspars group (framework silicates): alkali-feldspars ($\approx$ 3% microcline or orthoclase – $KAl_3Si_3O_8$) and calcium-bearing plagioclases ($\approx>$ 2% anorthite – $CaAl_2Si_2O_8$). The aggregate also contains traces of phyllosilicates in the form of biotite and chlorite.

Concrete Eleven (11) elemental maps were obtained in weight concentration for aluminum, calcium, iron, potassium, magnesium, manganese, sodium, phosphorus, sulfur, silicon and titanium. Magnesium, manganese, sodium, phosphorus, and sulfur were not observed because they lie on the detection limit of the instrument (e.g., sodium), or they appear only as traces. Calcium and silicon maps exhibit high weight concentrations characterizing, to a large extent, the hardened cement paste (hcp) and the aggregates, respectively in Fig. 2. The presence of calcium in moderate concentrations is also observed in some aggregates, likely indicating the presence of anorthite (An). Aggregates appearing in dark black in the silicon map are likely rich in quartz. Those appearing in gray also correspond to substantial amounts of iron and/or potassium, indicating the presence of phyllosilicates such as biotite and microcline or orthoclase.

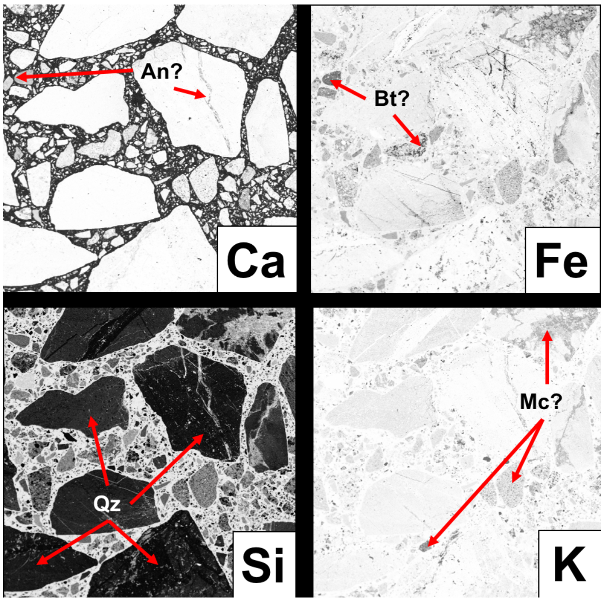

Figure 2: mXRF-derived weight concentration elemental maps (25.1 $\times$ 25.1 mm) for silicon, calcium, potassium and iron. An: anorthite, Bt: biotite, Mc: microcline, Qz: quartz.

4 PHASE ASSIGNMENT

4.1 DETERMINISTIC ANALYSIS

mXRF-based phase assignment relies on a set of logical and hierarchical rules[1] (priority order) established from the image analysis: (i) $[\mathrm{Ca}] \geq 0.5 \Rightarrow\sim$ hcp; (ii) $[\mathrm{Si}] \geq 0.67 \Rightarrow\sim$ Qz; (iii) $[\mathrm{K}] \geq 0.15 \wedge [\mathrm{Si}] \leq 0.67 \Rightarrow\sim (\mathrm{Mc} \vee \mathrm{Or})$; (iv) $[\mathrm{Fe}] \geq 0.353 \Rightarrow\sim$ Bt; (v) $[\mathrm{Ca}] \leq 0.5 \wedge [\mathrm{Ca}] \geq 0.14 \Rightarrow\sim$ An; with hcp: hardened cement paste, Qz: quartz, Mc: microcline, Or: orthoclase, An: anorthoclase and Bt: biotite.

The phase assignment is produced by MOSAIC using the *particles map*s approach: (i) All elemental maps are merged; (ii) A set of particles defined by areas of adjacent pixels of similar chemical composition is created. Each particle is assigned a phase using the logical rules defined above. Contiguous pixels forming the boundaries of a particle are not assigned to any phase in this study with the deliberate purpose of assigning specific mechanical bond properties between the hcp and aggregates, the so-called interfacial transition zone (ITZ), and also, between mineral "particles" within aggregates.

[1] $\wedge$: and, $\vee$: or, $\neg$: negation, $\sim$:likely, $\Rightarrow$: implies.

The output volume fractions obtained from the mXRF-based phase assignment and the relative volume fractions of mineral in aggregates (in bracket) of assigned phases are provided in Table 1. The mXRF-based estimated volume fraction of "pure" hcp is 20% compared with the 30% based on the fresh concrete composition. Given that about 15% of the pixels are unassigned and largely include ITZ pixels and intra-hcp pixels, the value of 20% is a very reasonable number. When specifically analyzing the volume fractions of rock-forming minerals relative to the fraction of aggregates, a good agreement with the Rietveld analysis is found, in particular with the most abundant phase, quartz (89% vs. 92%). The corresponding output phase map is presented in Fig. 3.

Table 1: Phase volume fractions derived from the mXRF data and comparison with data derived either from the concrete composition or XRD-Rietveld analysis. Data in brackets indicate volume fractions relative to the aggregates.

phase	mXRF	ref. data
		comp. ref.
hcp	20.3%	$\approx$30%
other†	14.9%	
		XRD
Qz	57.7% (89.0%)	64% (92%)
Mc	3.1% (4.8%)	5% (7.2%)
An	3.4% (4.5%)	
Bt	1.3% (1.6%)	<1%

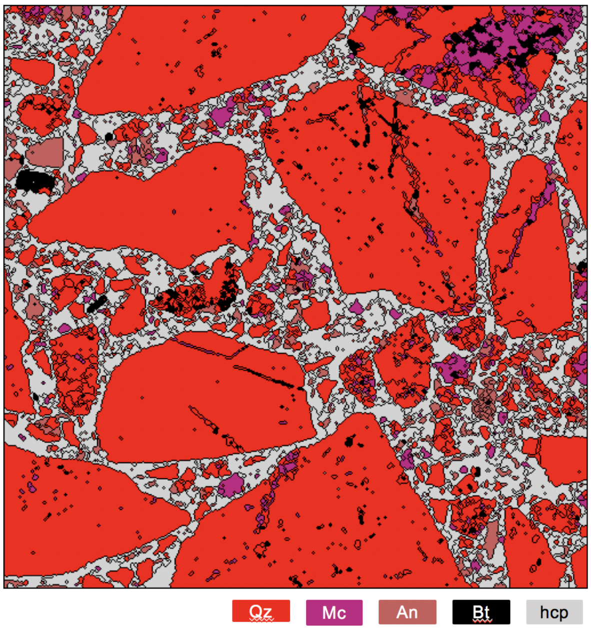

Figure 3: Concrete Con-A: mXRF-based output phase map (25.1 × 25.1 mm).

PROBABILISTIC ANALYSIS Acknowledging that the set of logical rules used in the assignment process relies somewhat on user-dependent threshold values, a probabilistic-based sensitivity analysis was conducted assuming that these threshold values were defined by uniform distributions: $\mathcal{U}[min; max]$. The distribution intervals were defined using *ImageJ*: (i) $[\mathrm{Ca}] \geq \mathcal{U}[0.470; 0.706] \Rightarrow\sim$ hcp; (ii) $[\mathrm{Si}] \geq \mathcal{U}[0.412; 0.667] \Rightarrow\sim$ Qz; (iii) $[\mathrm{K}] \geq \mathcal{U}[0.098; 0.255] \wedge [\mathrm{Si}] \leq \mathcal{U}[0.412; 0.667] \Rightarrow\sim$ $(\mathrm{Mc} \vee \mathrm{Or})$; (iv) $[\mathrm{Fe}] \geq \mathcal{U}[0.121; 0.392] \Rightarrow\sim$ Bt; (v) $[\mathrm{Ca}] \leq \mathcal{U}[0.470; 0.706] \wedge [\mathrm{Ca}] \geq \mathcal{U}[0.055; 0.176] \Rightarrow\sim$ An

1,000 MOSAIC simulations were launched from a *scilab* script to derive mean volume fractions and the relative standard deviations of the phases. The corresponding distributions are plotted in Fig. 4. Minor differences between the mean values obtained either by the deterministic or the probabilistic analyses (Tab. 2) can be observed, which is extremely reassuring given the significant extent of the threshold distribution intervals. The output volume fractions of hcp, quartz and the total fraction of remaining minerals were found to be relatively insensitive to the chosen concentration thresholds. What changed from one simulation to another was primarily the manner in which minor phases—microcline, anorthite and biotite—are distributed in the microstructure.

Table 2: Comparison of the phases volume fractions derived from the deterministic and probabilistic analysis.

phase	deterministic	probabilistic	
		mean	(std.)
hcp	20.3%	19.5%	(0.7%)
Qz	57.7%	57.5%	(2.2%)
Mc	3.1%	2.4%	(1.2%)
An	3.4%	3.9%	(1.3%)
Bt	1.3%	1.8%	(1.3%)

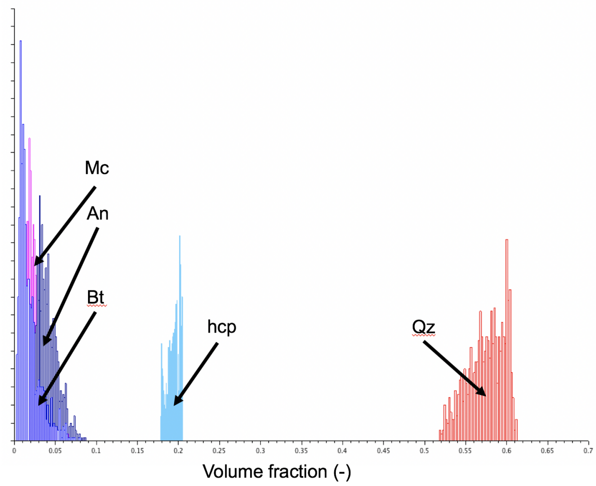

Figure 4: Concrete Con-A: distribution of phases volume fractions obtained from the sensitivity analysis.

5 IRRADIATION SIMULATION

5.1 FFT-BASED SIMULATION

The complexity and high resolution of the mXRF-based microstructure are almost impossible to handle through classical finite elements method (FEM) because the computational time to simulate large-scale microstructures would be prohibitive to use in practice due to the complexity of the coupled creep-damage algorithm. Alternatively, fast Fourier transform (FFT)-based simulation of periodic heterogeneous mediums alleviates FEM limitations [8, 9]. MOSAIC's solver uses the accelerated algorithm developed by [10] for elastic problems, later extended to viscoelasticity in [11] and to eigenstrains in the present work. MOSAIC uses a sequential nonlinear solver to compute the damage propagation in the microstructure. The damage algorithm is nonlocal in order to limit spurious oscillations arising from the FFT calculations and to reduce the sensitivity of the method to the spatial discretization. MOSAIC is linked to the LWRS-developed IMAC (Irradiated Minerals, Aggregates and Concrete) database that includes physical and mechanical properties of nonirradiated and irradiated minerals such as the elemental and chemical composition, density, and elastic constants tensors.

5.2 CONSTITUTIVE MODEL

Coupled Damage Creep From the very limited data on creep of irradiated cementitious materials available in the open literature [12, 13], it is suspected that neutron irradiation may accelerate the basic creep rate in hcp, while gamma-irradiation–induced radiolysis affects drying creep by accelerating water loss. In the proposed model, shrinkage is currently neglected, and only the unirradiated hcp basic creep rate is considered. Cement paste creep is simulated with an aging logarithmic model, assuming a separation of the short-term recoverable creep ε_r and the long-term nonrecoverable creep ε_c. The rheological model [14] is thus composed by an elastic spring in series with a Kelvin-Voigt unit (short-term creep) and a time-dependent dashpot (long-term creep), as with the B3 model [15] or the model more recently proposed by Hilaire et al. [16]. The time-dependent dashpot models the long-term logarithmic creep consistently with the observation of concrete and cementitious materials, both at the nanoscale [17] and the macroscale [18]. The Kelvin-Voigt unit allows a partial recovery of the creep strains upon unloading, as identified in experimental campaigns [19].

Model The corresponding set of constitutive differential equations is as follows:

$$\begin{aligned} \sigma &= (1-d)\mathbf{C}_e : [\varepsilon - \varepsilon_r - \varepsilon_c - \varepsilon^*] \\ \sigma &= (1-d)\left[\mathbf{C}_r : \varepsilon_r + \mathbf{E}_r : \dot{\varepsilon} - r\right] \\ \sigma &= (1-d)\left[1 + \frac{t}{\tau_c}\right]\mathbf{E}_c : \dot{\varepsilon}_c, \end{aligned} \tag{1}$$

where $\mathbf{C}_e$ is the elastic stiffness tensor of the phase; $\mathbf{C}_r$ and $\mathbf{E}_r$ are the hcp stiffness and viscosity tensors of the Kelvin-Voigt module, respectively; $\mathbf{E}_c$ is the initial viscosity tensor of the dashpot; ε^* is the imposed deformation (i.e., shrinkage, RIVE, and thermal strains); and τ_c is the characteristic time of the logarithmic creep.

Rock-forming minerals RIVE RIVE results from the amorphization of minerals, in which gradual disorder generally leads to a decreasing density [20]. RIVE often evolves as a sigmoidal function of the neutron fluence [21]. However, increasing irradiation temperature affects RIVE rate by promoting *point-defect annealing*, or *irradiation annealing* [20, 22] The rate of expansion varies in each phase as a function of fluence and irradiation temperature. Irradiation-induced volume expansion in rock-forming minerals is assumed isotropic in each *particle*. The RIVE parameters for the minerals present in the studied microstructure have been derived from the literature data gathered in Denisov et al. [23] and analyzed in Le Pape et al. [5].

5.3 IRRADIATION EXPERIMENTS

The detailed description of the irradiation experiments can be found in Maruyama et al. [4]. Concrete cylinders that are 4 cm in diameter were exposed to irradiation in the Institute for Energy Technology (IFE) JEEP-II test reactor (Kjeller, Norway). Only specimen A10 in capsule PPT-D is modeled here: the final fluence is 0.768 $\mathrm{n.pm}^{-2}$ ($E > 10$ MeV) after 182 days of accelerated testing [4, Tab. 16, p. 455] (neutron spectrum provided by Pr. Maruyama). The neutron flux and irradiation temperature of 67 °C are assumed steady, not accounting for the reactor cycles, and the specimen is uniform, not accounting for the energy deposition gradient. The RIVE of the concrete specimen is unrestrained.

5.4 RESULTS

The simulation of the irradiation experiment is summarized in Fig. 5. The thick solid line shows the dimensional change with increasing fluence. The expansion of concrete, largely dominated by quartz RIVE, compares well with post-irradiation examination (PIE) data for fluence in the range of 0.1–0.3 $\mathrm{n.pm}^{-2}$ ($E > 10\ \mathrm{MeV}$), but it tends to underestimate the actual expansion for fluence $> 0.7\ \mathrm{n.pm}^{-2}$. At an early stage, localized damage appears to initiate in the hcp prominently between close aggregates and at the interfaces between aggregate *particles*. Note that all interface elements in this preliminary simulation have been assigned the constitutive model of hcp, which causes early cracking at the boundaries between rock-forming minerals *particles*. At an intermediate stage, initially formed localized damage tends to diffuse from those areas in the hcp, or it propagates further along the aggregate *particle* interfaces. At a later stage, damage propagates entirely to the hcp. Damage, in the sense of its average value in the hcp, progresses rapidly to its full extent— $< d_{\mathrm{hcp}} > \approx 1$—reached at $\approx 0.3\ \mathrm{n.pm}^{-2}$. This rapid development is possibly an artifact of 2D simulation promoting premature cracking percolation [24].

6 CONCLUSION AND PERSPECTIVES

This research demonstrates that imaging characterization techniques of unirradiated concrete provide critical input into the MOSAIC platform that is used to evaluate concrete susceptibility to damage by RIVE. The result is the development of a methodology to derive high-resolution minerals phase maps from combined characterization techniques. These techniques include (i) petrographic analysis using transmitted and cross-polarized light microscopy to define a list of minerals of high interest, (ii) XRD quantification (powder) of the average mineral volume fractions in the aggregates, and (iii) mXRF-based maps (weight concentration) of the elements heavier than magnesium. Using MOSAIC, the varied elemental maps are combined and interpreted in terms of inference rules that lead to high-resolution mineral phase maps that can be directly used in MOSAIC-IMAC simulation modules. The intrinsic irradiated properties of each mineral phase are directly obtained from a previous comprehensive analysis of literature data. The first-of-a-kind simulation of an actual irradiation experiment of concrete in the JEEP-II test reactor shows the predictive capability of the proposed approach in terms of irradiation-induced expansion of concrete when compared with PIE data. The development of simulated irradiation-induced damage requires further validation, as related PIE data are not yet available.

Further numerical developments, experimental research, and validation are needed to pursue this work, including (i) validating the proposed to more complex aggregate microstructure; (ii) expanding MOSAIC's capabilities to 3D modeling in conjunction with computerized x-ray tomography-based characterization; and (iii) conducting neutron-irradiated creep experiments on hcp to efficiently account for the distribution of energy release through cracking and stress-relaxation [14].

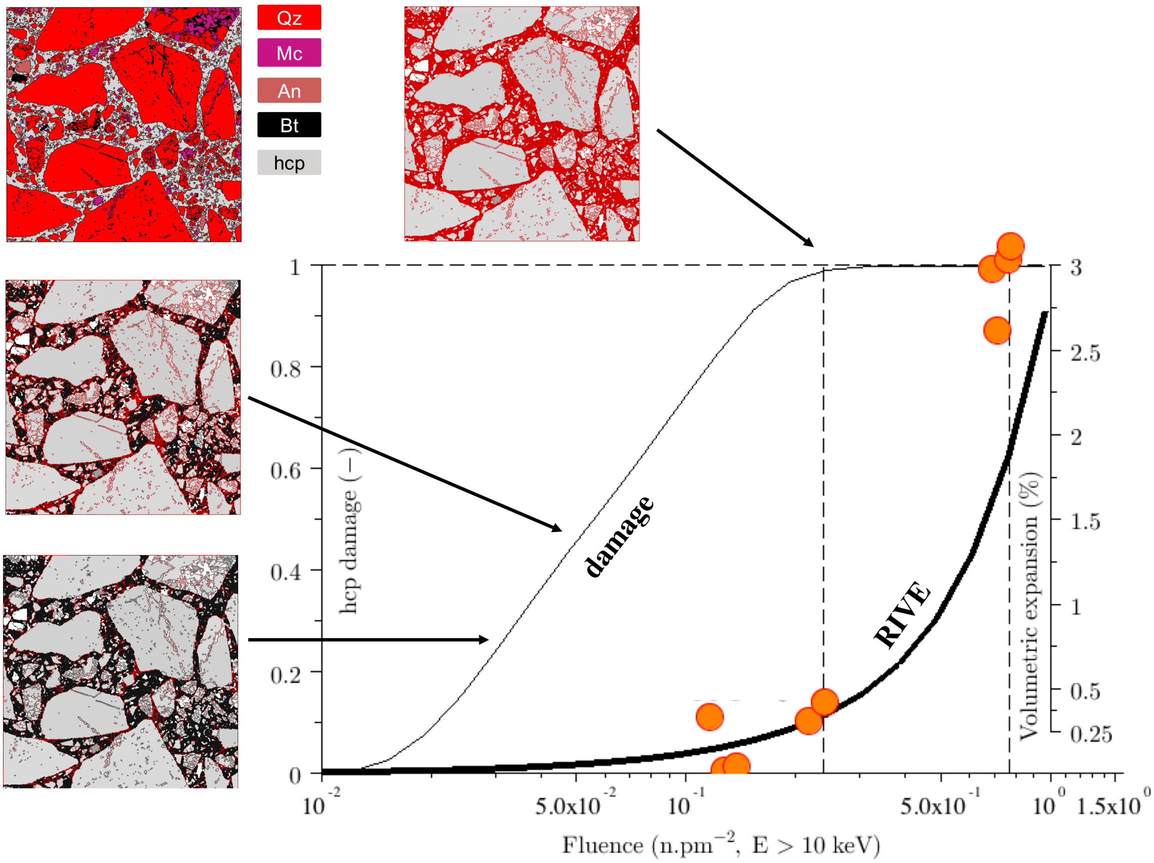

Figure 5: Evolution of RIVE (thick solid line) and damage (thin solid line) during irradiation. Orange circles indicate re-interpreted PIE dimensional change data [4]. Red pixels in the surrounding stiffness maps indicate the location of irradiation-induced damage.

ACKNOWLEDGEMENT

This material is based upon work supported by the US Department of Energy Office of Nuclear Energy Light Water Reactor Sustainability Program under contract number DE-AC05-00OR22725. The authors would like to express their gratitude to the Japan Concrete Aging Management Program-related researchers, Pr. I. Maruyama (Nagoya University), Dr. Takizawa (Mitsubishi Research Institute) and Dr. Kontani (Kajima Corp.) for sharing the unirradiated concrete specimens that made this research possible.

References

[1] H.K. Hilsdorf, J. Kropp, and H.J. Koch. The effects of nuclear radiation on the mechanical properties of concrete. *Special Publication of The American Concrete Institute*, 55:223–254, 1978.

[2] J. Seeberger and H.K. Hilsdorf. Einfluß von radioactiver Strahlung auf die Festogkeit and Struktur von Beton. Technical Report NR 2505, Institut für Massivbau and Baustofftechnologie, Universität Karlsruhe, 1982.

[3] Y. Le Pape, K.G. Field, and I. Remec. Radiation effects in concrete for nuclear power plants – Part II: Perspective from micromechanical modeling. *Nuclear Engineering and Design*, 282:144–157, 2015.

[4] I. Maruyama, O. Kontani, M. Takizawa, S. Sawada, S. Ishikawa, J. Yasukouchi, O. Sato, J. Etoh, and T. Igari. Development of the soundness assessment procedure for concrete members affected by neutron and gamma-irradiation. *Journal of Advanced Concrete Technology*, 15:440–523, 2017.

[5] Y. Le Pape, M.H.F. Alsaid, and A.B. Giorla. Rock-forming minerals radiation-induced volumetric expansion – revisiting the literature data. *Journal of Advanced Concrete Technology*, 16:191–209, 2018.

[6] H. Graves, Y. Le Pape, D. Naus, J. Rashid, V. Saouma, A. Sheikh, and J. Wall. Expanded material degradation assessment (EMDA), volume 4: Aging of concrete. Technical Report NUREG/CR-7153, ORNL/TM-2011/545, U.S. Nuclear Regulatory Commission, 2014.

[7] G. Igarashi, I. Maruyama, Y. Nishioka, and H. Yoshida. Influence of mineral composition of siliceous rock on its volume change. *Construction and Building M*, 94:701–709, SEP 30 2015.

[8] H. Moulinec and P. Suquet. A fast numerical method for computing the linear and nonlinear mechanical properties of composites. *Compte Rendus de l'Académie des Sciences, Série H. Mécanique, physique, Chimie, Astronomie*, 318(11):1417–1423, 1994.

[9] H. Moulinec and P. Suquet. A numerical method for computing the overall response of nonlinear composites with complex microstructure. *Computer methods in applied mechanics and engineering*, 157(1):69–94, 1998.

[10] V. Monchiet and G. Bonnet. A polarization-based FFT iterative scheme for computing the effective properties of elastic composites with arbitrary contrast. *International Journal for Numerical Methods in Engineering*, 89(11):1419–1436, 2012.

[11] F. Lavergne, K. Sab, J. Sanahuja, M. Bornert, and C. Toulemonde. Investigation of the effect of aggregates' morphology on concrete creep properties by numerical simulations. *Cement and Concrete Research*, 71:14–28, 2015.

[12] B.S. Gray. The effects of reactor radiation on cement and concrete. In *Proceedings of an Information Exchange Meeting*

on 'Results of Concrete Irradiation Programmes', volume EUR 4751 f-e, Brussels, Belgium, April 19 1971. Commission des Communautés Européennes.

[13] D.C. McDowall. The effects of gamma radiation on the creep properties of concrete. In *Proceedings of an Information Exchange Meeting on 'Results of Concrete Irradiation Programmes'*, volume EUR 4751 f-e, pages 55–69, Brussels, Belgium, April 19 1971. Commission des Communautés Européennes.

[14] A. Giorla, Y. Le Pape, and C. Dunant. Computing creep-damage interactions in irradiated concrete. *Journal of Nanomechanics and Micromechanics*, 04017001, 2017. Accepted.

[15] Z.P. Bažant and S. Baweja. Creep and shrinkage prediction model for analysis and design of concrete structures: Model B3. *ACI Special Publication*, 194:1–84, 2000.

[16] A. Hilaire, F. Benboudjema, A. Darquennes, Y. Berthaud, and G. Nahas. Modeling basic creep in concrete at early-age under compressive and tensile loading. *Nuclear Engineering and Design*, 269:222–230, 2014.

[17] M. Vandamme and F.-J. Ulm. Nanogranular origin of concrete creep. *Proceedings of the National Academy of Sciences*, 106(26):10552–10557, 2009.

[18] Z. Bažant, Q. Yu, and G. Li. Excessive long-time deflections of prestressed box girders. I: Record-span bridge in palau and other paradigms. *Journal of Structural Engineering*, 138(6), 2012.

[19] A. Bengougam. *Déformations différées et effet d'échelle des bétons de barrage*. PhD thesis, École Polytechnique Fédérale de Lausanne, 2002.

[20] W Primak. Fast-neutron-induced changes in quartz and vitreous silica. *Physical Review*, 110(6):1240–1254, 1958.

[21] V.G. Zubov and A.T. Ivanov. Expansion of quartz caused by irradiation with fast neutrons. *Soviet Physics Crystallography*, 11(3):372–374, 1966.

[22] V.N. Bykov, A.V. Denisov, V.B. Dubrovskii, V.V. Korenevskii, G.K. Krivokoneva, and L.P. Muzalevskii. Effect of irradiation temperature on the radiation expansion of quartz. *Atomnaya Energiya*, 51(3):593–595, September 1981.

[23] A.V. Denisov, V.B. Dubrovskii, and V.N. Solovyov. *Radiation Resistance of Mineral and Polymer Construction Materials*. ZAO MEI Publishing House, 2012. in Russian.

[24] A. Giorla, M. Vaitová, Y. Le Pape, and P. Štemberk. Meso-scale modeling of irradiated concrete in test reactor. *Nuclear Engineering and Design*, 295:59–73, 2015.